ELSEVIER

Journal of Structural Geology 26 (2004) 1361–1376

JOURNAL OF STRUCTURAL GEOLOGY

www.elsevier.com/locate/jsg

Deformation of square objects and boudins

Susan H. Treagus[a,*], Labao Lan[b]

[a]*Department of Earth Sciences, University of Manchester, Manchester M13 9PL, UK*
[b]*IRI/The Earth Institute, Columbia University, Palisades, NY 10964-8000, USA*

Received 21 August 2003; received in revised form 1 December 2003; accepted 9 December 2003

Available online 3 February 2004

Abstract

Some geological objects, such as clasts and boudins, may have had original shapes close to square, that have been modified by ductile deformation. We demonstrate through finite element models presented here and in earlier papers that square objects in a matrix with contrasting viscosity can deform to a variety of curved shapes. The maximum shape change is where the square edges are parallel to the principal bulk strains. Competent objects with viscosity ratio to matrix (m) of 2–20 become barrel shaped, showing concave 'fish mouth' shortened edges. Incompetent objects ($m < 1$) show a narrower variety of shapes with m, all becoming smoothed to bone, dumb-bell or lobate shapes, and losing the original corners.

We compare the results for square objects with linear and non-linear rheology (power law, stress exponent $n = 1$, 3 or 10), and with previous modelling with different object–matrix proportions. Competent objects with higher n values deform slightly less, and more irregularly, than linearly viscous ($n = 1$) objects, but the distinctions between $n = 3$ and 10 are only slight. The differences are even slighter (in the opposite sense) for incompetent objects. The proportion of object to matrix is as important, if not more, in controlling the deformation and shape of these objects. The results are compared via graphs of object strain and concavity versus bulk strain.

The concavity graph for competent square objects with linear viscosity up to very high strain can be compared with examples of ductile boudins with barrel or fish mouth shapes. Subject to a number of assumptions, this provides a method of estimating boudin–matrix viscosity ratios and post-boudinage ductile strain, of potential use in highly deformed rocks lacking other strain markers. The approach may also be suitable for deformed porphyroblasts, but is more difficult to apply to single clasts in breccias and conglomerates.

Keywords: Finite element modelling; Square objects; Boudins; Rheology

1. Introduction

The deformation of square objects may not, at first, seem as relevant to geological deformation as the deformation of circular or elliptical objects. In sedimentary rocks, most grains or clasts are rounded to some degree, and objects classically used as strain markers, ooids, lapilli and reduction spots, were probably originally close to circular. However, clasts in conglomerates and breccias can often be irregular or angular in shape, and porphyroclasts in metamorphic rocks are commonly square or rectangular in section (e.g. feldspar). Another class of geological object that is square to rectangular in cross-section is a boudin.

There is an important difference between the two-dimensional deformation of isolated elliptical and non-elliptical objects in a matrix, where the object has a different viscosity from its surrounding matrix. Elliptical objects deform homogeneously into other ellipses, retaining the elliptical geometry, even when the strain is different from the matrix strain. On the other hand, non-elliptical objects deform heterogeneously to a variety of shapes. We have demonstrated this for square objects in a matrix, through finite element modelling (Treagus et al., 1996; Treagus and Lan, 2000, 2003). The squares become barrel-shaped with concave shortened edges, for objects that are more viscous than the matrix (Fig. 1); they become bone or dumb-bell shapes in objects that are less viscous than the matrix. In these earlier FEM studies, we examined and quantified shape changes for square objects in different orientations in pure shear and in simple shear, where the object and matrix were both Newtonian and in perfect coherence. The maximum shape changes and irregularity are seen in square objects with sides parallel to the principal

* Corresponding author. Tel.: +44-161-275-3804; fax: +44-161-275-3947.

E-mail address: susan.h.treagus@man.ac.uk (S.H. Treagus).

0191-8141/$ - see front matter © 2004 Elsevier Ltd. All rights reserved.
doi:10.1016/j.jsg.2003.12.002

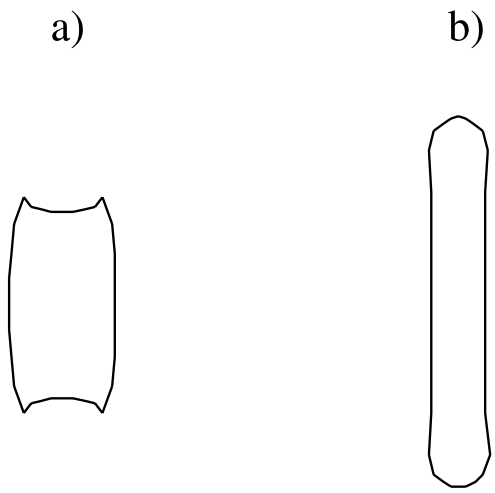

Fig. 1. Shapes of deformed square objects, after Treagus and Lan (2000), both after pure shear with bulk strain ratio of $R_B = 4$ (50% shortening). (a) Competent object ($m = 5$). (b) Incompetent object ($m = 0.1$).

axes of strain, as illustrated in Fig. 1. The present paper extends this work with new modelling of square objects in a matrix, comparing results for objects that are linearly and non-linearly viscous, the latter with a power law rheology.

Compilations of laboratory rock deformation studies (e.g. Carter and Tsenn, 1987; Kirkby and Kronenberg, 1987; Rutter, 1993) show that many rocks obey non-linear flow laws that are sensitive to the deformation mechanism, leading to extrapolations that natural rocks flow non-linearly according to a power law, with stress exponent (n) in the order of three or more. However, power law rheology still remains to be proved by the geological structures that form during *natural* ductile deformation of rocks. The viscosity ratios deduced from cleavage refraction (Treagus, 1999), and those determined from strain variations in conglomerates (Gay, 1968; Lisle et al., 1983; Treagus and Treagus, 2002), all show rather small values within about an order of magnitude, which is more suggestive of quasi-Newtonian flow for a range of common rock types during ductile deformation than of power law flow. We clearly need good structural criteria to indicate rock rheology that can complement results of laboratory rock deformation. One of the purposes of this paper is to reveal whether deformed *square objects* might provide such a rheological criterion.

The most striking parallel to the barrel shapes of deformed competent square objects (e.g. Fig. 1) are some of the shapes described for geological boudins. Boudins have a variety of geometric forms, but Wegmann (1932), Cloos (1947), Ramberg (1955) and many subsequent publications describe a class of boudin that is barrel-shaped with concave ends (Fig. 2). These are considered indicative of ductile or plastic deformation of originally rectangular or square boudins during protracted deformation and metamorphism. In some cases, the shapes of the shortened concave ends are so extreme that they show 'horn-like protuberences' (Lloyd and Ferguson, 1981), or can be described as having a 'fish head' or 'fish mouth' form (Ghosh, 1993, p. 387; Ramsay and Lisle, 2000, p. 995). These concave end regions (which in a string of boudins is called the inter-boudin gap) are most commonly seen in gneisses (e.g. Fig. 2b and c), where they are sometimes filled with vein quartz or pegmatite.

Barrel to 'fish-mouth' shapes analogous to boudins have been simulated in deformed *rectangular objects* in a matrix, by elastic–plastic FEM (Lloyd et al., 1982) and by linearly viscous modelling (Ramsay and Lisle, 2000, fig. 39.19), and in deformed *square objects* in a matrix by linearly viscous FEM (Treagus et al., 1996; Treagus and Lan, 2000). In the latter paper, we introduced a convexity/concavity factor, C, to define the end shape in terms of the model strain, which might provide a practical measure of the viscosity ratio of object to matrix, of possible application to geological clasts and boudins. This approach will be pursued in the present paper, which investigates linear and non-linear viscosity of square objects. We attempt to apply the results to rocks, in the hope of fulfilling Ramberg's (1955, p. 513) prediction that "studies of boudinages could provide an excellent key to…the rheological characteristics of rocks".

2. Finite element models

We use a two-dimensional finite element program, developed by Hanson (1990) for non-linear flow in ice, and modified for geological applications by Lan and Hudleston (1991). A detailed description of the equations and modification of the program can be found in a series of papers (Lan and Hudleston, 1991, 1996, 1997; Hudleston and Lan, 1994), and recent explanations of the program and model were also given by Treagus and Lan (2003). This program has been used to produce a series of finite element models of structures with Newtonian or power-law rheologies (Hudleston and Lan, 1993, 1994; Lan and Hudleston, 1996, 1997; Treagus et al., 1996; Treagus and Lan, 2000; Treagus and Lan, 2003), and hence is used for the models in this paper. A velocity boundary condition is used in all our models, according to established finite element theory (Zienkiewicz and Taylor, 2000), and justified recently by Treagus and Lan (2003).

The two-dimensional finite element model follows the design of the 'quarter model' used by Treagus et al. (1996): quarter of a square inclusion (object) enclosed in a matrix in pure shear (Fig. 3a). A different 'full square model' (Fig. 3b) was investigated by Treagus and Lan (2000), as part of a study of pure shear of square objects in symmetric and asymmetric orientations. The purpose of the present paper is to investigate the changes in shape when objects have a power-law rheology with different values of power-law stress exponent, n. As the maximum shape changes in earlier models were seen in square objects with their sides parallel to the principal far-field strain axes (e.g. Fig. 1), our present FE models only concern this orientation of square

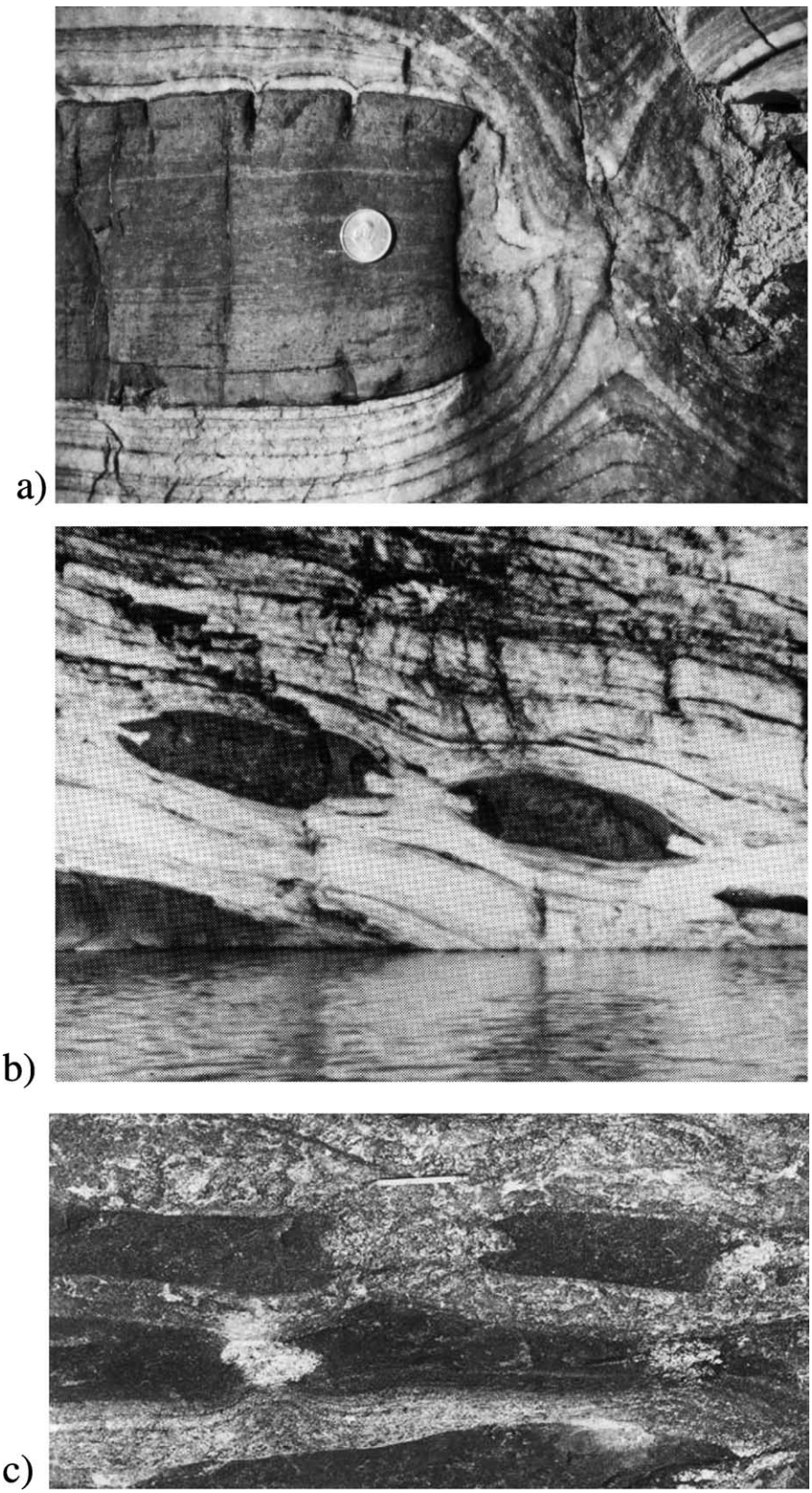

Fig. 2. Natural boudins with barrel to 'fish mouth' sectional shapes. (a) Boudin in calc–silicate layer in marble, Khan Gorge, Namibia, courtesy of J.G. Ramsay (see Ramsay, 1967, fig. 3-43; Ramsay and Lisle, 2000, fig. 37.11). Coin for scale. (b) Boudined amphibolite dyke in quartzo-feldspathic gneiss (Lloyd et al., 1982, fig. 2b), courtesy of A.E. Wright, from Sermiligaq fjord, east Greenland (Wright et al., 1973). Boudins are metres long (exact scale not known). (c) Fish head boudins in amphibolite bands in quartzo-feldspathic gneiss matrix in the Jashidih area of migmatites, east India (Ghosh and Sengupta, 1999), courtesy of S. Sengupta. Pencil for scale.

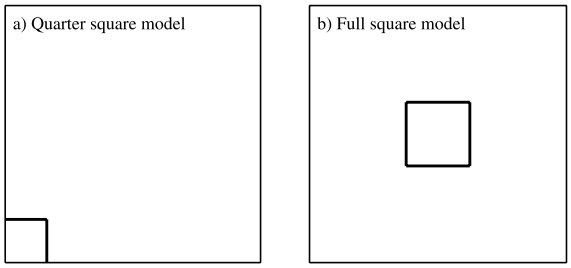

Fig. 3. Previous finite element models of a square object in a matrix. (a) Quarter model of Treagus et al. (1996), and used in this paper. (b) Full square model with larger object to matrix ratio, used by Treagus and Lan (2000).

objects in pure shearing, for which there is four-fold symmetry and thus quarter models are sufficient.

The FE model comprises 190 triangular or quadratic elements, 25 in the object and 165 in the matrix (Fig. 4a). The whole model is initially six units square, and the object is one unit square, occupying 1/36 the model area. Time steps (increments of model deformation) are 0.05 unit shortening displacement, and results are compared after 30, 60, 80 and 90 increments, equivalent to bulk pure shear strain ratios of $R_B = 1.78$, 4, 9 and 16. Some of the $n = 1$ models were deformed to even greater strains (95 and 99 increments, $R_B = 23$ and 32.7) to examine extreme object shape irregularity. In all the models, there is perfect coherence and continuity at the object–matrix boundary.

The matrix of the models is treated as a Newtonian fluid, and the object as a power-law fluid with the flow law: $\dot{\epsilon} = D\sigma^n$, where $\dot{\epsilon}$ and σ are the effective strain rate and effective stress (second invariants of the strain rate and deviatoric stress tensors, respectively), n is the stress exponent, and D is a constant expressing the viscosity (see Lan and Hudleston, 1991). The effective viscosity ratio (m) of power law objects to the Newtonian viscous matrix is measured as the viscosity ratio of the two media at the initial bulk strain rate of the models.

In the previous full-square models of Treagus and Lan (2000) (Fig. 3b), where object and matrix are both Newtonian ($n = 1$), we found the greatest shape irregularity for the $m = 5$ models. We have therefore concentrated most of our modelling of competent shape changes on m values of 10, 5 and 2, and use n values of 1, 3 and 10 as for previous non-linear modelling (Lan and Hudleston, 1991). For modelling incompetent objects, we use $m = 0.1$ only. It was revealed in earlier modelling (Treagus and Lan, 2000, 2003), that very similar shapes were produced for incompetent objects in the range $0.1 \geq m \geq 0.001$, showing that the results were not very sensitive to m, when < 1, and that there is a maximum deformation that sets a 'limit of incompetence'. For this reason, and because the geological applications for incompetent objects are less obvious than for competent objects, we have not investigated other values of $m < 1$ here.

3. Model results

The FEM configuration is illustrated in Fig. 4, in a model with an object/matrix viscosity contrast of $m = 5$ and three different object n values (1, 3, 10). The initial geometry of elements is shown, and then their appearance after pure

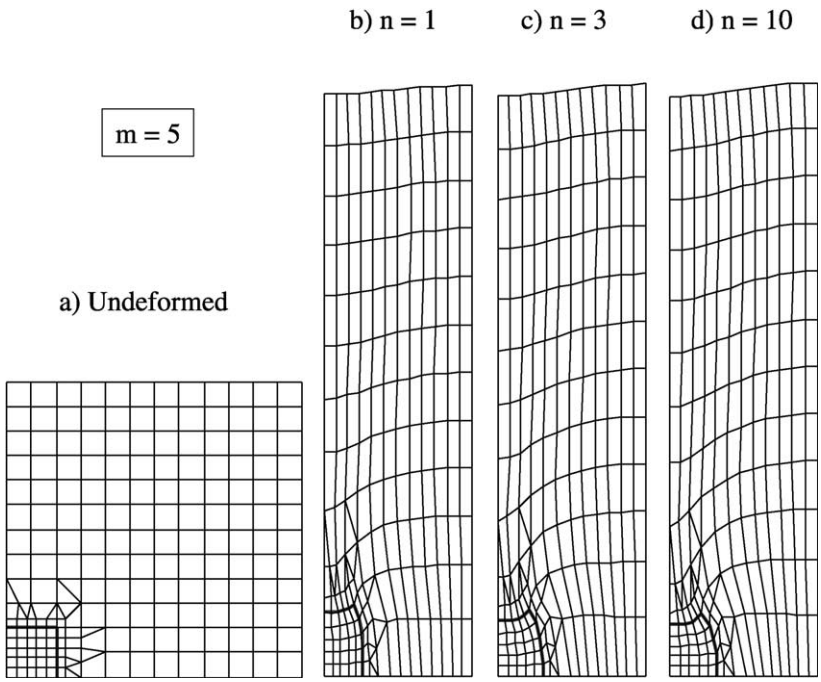

Fig. 4. Configuration of elements in the finite element model (quarter model). (a) Initial model with the square object outlined in bold. (b)–(d) Models with an object/matrix viscosity ratio of $m = 5$, after bulk pure shear deformation (strain ratio of $R_B = 4$), for objects with different values of power law with stress exponent, n: (b) $n = 1$ (Newtonian), (c) $n = 3$ and (d) $n = 10$.

shear with 50% model shortening. The object outlines are shown in bold, illustrating the shape change of a competent square object to a characteristic (quarter) barrel shape. The heterogeneous deformation in the matrix is indicated by the curved gridlines. Differences in object shapes are seen for different n values in Fig. 4, with the $n = 10$ model appearing the least deformed as a whole (less inequant), and the most irregular in shape.

In this paper, we are interested in the shape changes of quarter-objects from square, and the effect of different object n values. Thus, the rest of our FEM results will concentrate on showing only the outlines of the objects, for different m and n values in increasing degree of pure shear (Figs. 5–8). Object shape changes are superimposed for progressive deformation given by bulk pure shear strain ratios of $R_B = 1$ (initial square), 1.78 (25% shortening), 4 (50% shortening), 9 (67% shortening), and 16 (75% shortening), which is the limit used in models with power-law rheology. In each figure, (a) is the shape change for a passive marker with no viscosity contrast to the matrix (i.e.

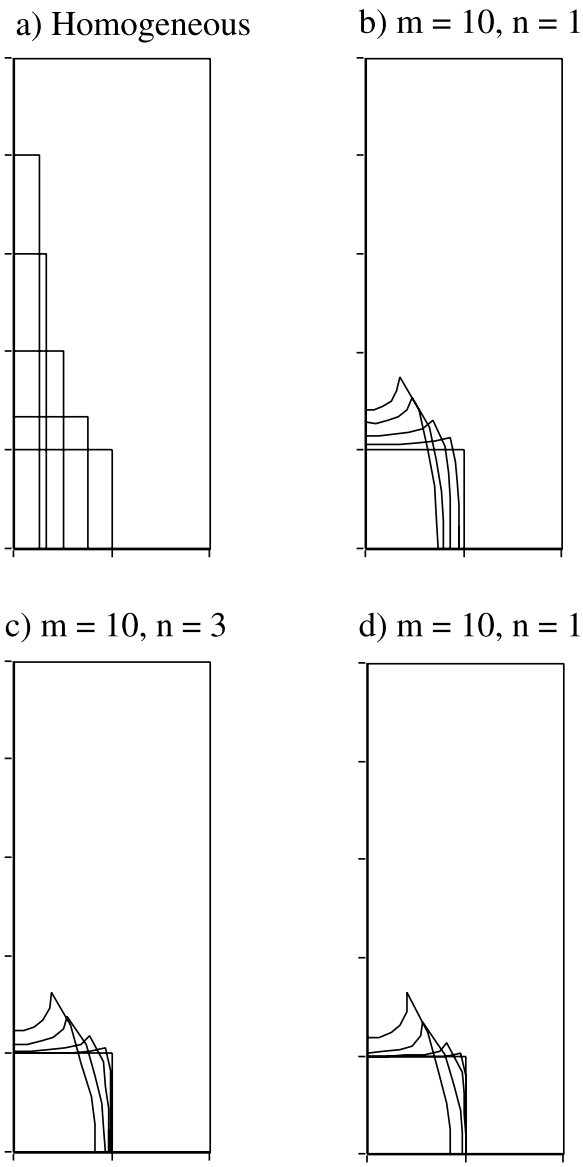

Fig. 5. Shape changes of square objects in a matrix in successive stages of pure shear with bulk pure shear strain ratios of $R_B = 1$ (initial square), 1.78 (25% shortening), 4 (50% shortening), 9 (67% shortening) and 16 (75% shortening). (a) Homogeneous deformation of passive objects, indicating bulk deformation. (b) and (c) Deformation of competent objects with viscosity ratio of $m = 10$, and stress exponent (n) of 1, 3 and 10, respectively. Note that the object deformation is much less than the bulk deformation, the squares become barrel-shaped, and the corners become 'horned'.

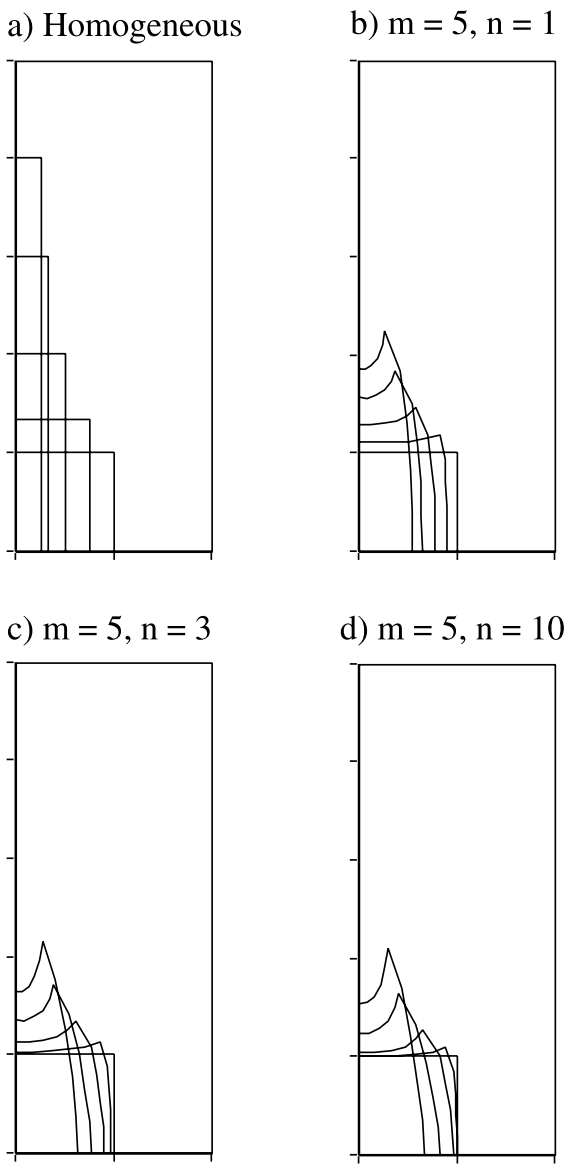

Fig. 6. Shape changes of square objects in a matrix in successive stages of pure shear with bulk pure shear strain ratios of $R_B = 1$ (initial square), 1.78 (25% shortening), 4 (50% shortening), 9 (67% shortening) and 16 (75% shortening). (a) Homogeneous deformation of passive objects, indicating bulk deformation. (b) and (c) Deformation of competent objects with viscosity ratio of $m = 5$, and stress exponent (n) of 1, 3 and 10, respectively. Note that the object deformation is less than the bulk deformation, the squares become barrel-shaped, and the shortened edges highly concave to produce a 'fish mouth'.

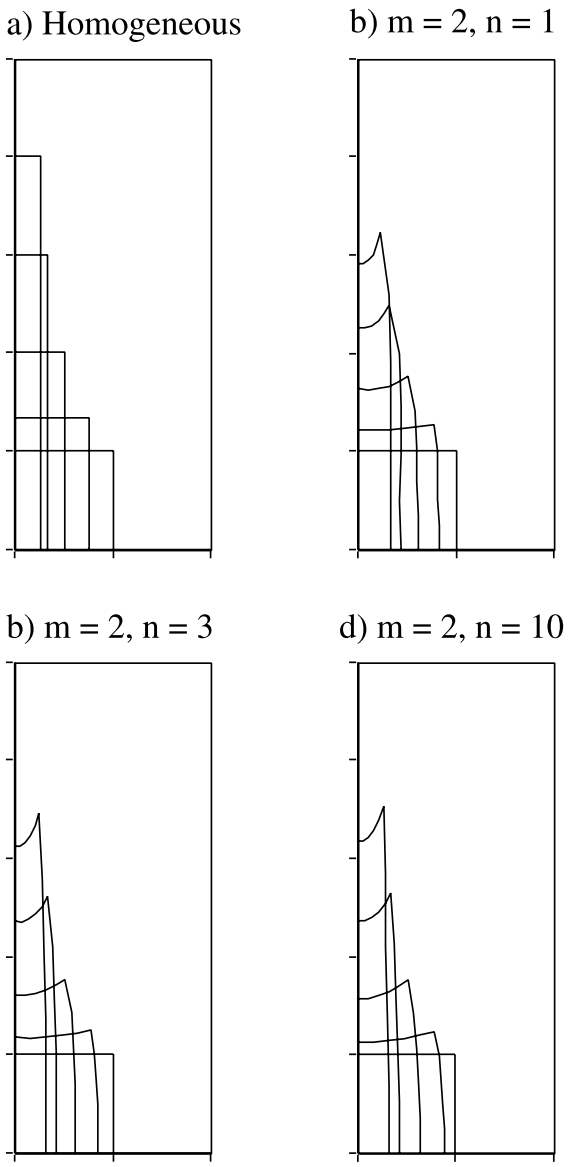

Fig. 7. Shape changes of square objects in a matrix in successive stages of pure shear with bulk pure shear strain ratios of $R_B = 1$ (initial square), 1.78 (25% shortening), 4 (50% shortening), 9 (67% shortening) and 16 (75% shortening). (a) Homogeneous deformation of passive objects, indicating bulk deformation. (b) and (c) Deformation of slightly competent objects with viscosity ratio of $m = 2$, and stress exponent (n) of 1, 3 and 10, respectively. Note that the object deformation is slightly less than the bulk deformation, and the shortened edges are concave.

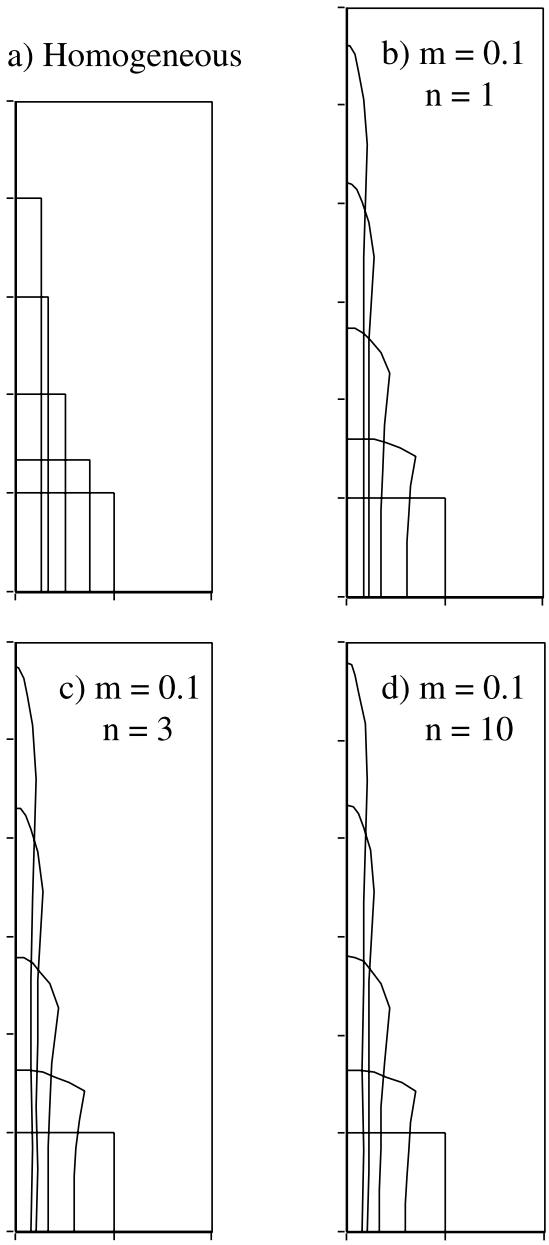

Fig. 8. Shape changes of square objects in a matrix in successive stages of pure shear with bulk pure shear strain ratios of $R_B = 1$ (initial square), 1.78 (25% shortening), 4 (50% shortening), 9 (67% shortening) and 16 (75% shortening). (a) Homogeneous deformation of passive objects, indicating bulk deformation. (b) and (c) Deformation of incompetent objects with viscosity ratio of $m = 0.1$, and stress exponent (n) of 1, 3 and 10, respectively. Note that the object deformation is more than the bulk deformation, the squares become (quarter) spatula to dumb-bell to lobate strip shapes, the corners disappear, and the shortened edge is highly convex and quasi-elliptical-shaped.

homogeneous deformation), that is then compared with (b)–(d) for a particular model m value and object n values of 1, 3 and 10, respectively.

The *competent objects* with $m = 10$ (Fig. 5) deform noticeably less than passive objects, but all develop 'horns' at leading corners. Both the power-law examples (Fig. 5c and d) remain almost square until $R_B > 4$, with the differences between $n = 3$ and 10 very small. The $m = 10$, $n = 10$ object develops the greatest horning or fish-mouth shape, more so than the linear ($n = 1$) object. Similar trends are seen in Fig. 6 for $m = 5$, but the objects as a whole deform more here than in the $m = 10$ examples. Strongly horned fish-mouth shapes of the shortened object edges are seen, with concave shortened edges that are approximate elliptical curves. The most mildly competent objects, those with $m = 2$ (Fig. 7), deform less than passive objects, but with less extreme shape irregularity than for $m = 5$ or 10. For the first two stages of deformation,

the power-law objects deform slightly less than the linear object, as seen in the previous examples. However, at the more extreme stages of deformation, the opposite is seen. Now, the power-law objects (Fig. 7c and d) have overtaken the deformation of the linear object and appear to behave less competently than the $n = 1$ object. This change in relative competence will be explained below. All these competent object shape changes (barrel to fish mouth) are similar to those described earlier for square objects with linear viscosity (Treagus et al., 1996; Treagus and Lan, 2000). Exact comparisons among these new models and previous models will be made in the next section.

We use $m = 0.1$ only, to model *incompetent objects* with different values of power-law exponent n, for reasons given above. The results in Fig. 8 show objects that have deformed more than passive homogeneous objects, but with only slightly more deformation as n increases. The most distinct feature of these incompetent models is the progressive disappearance of the square shape during progressive deformation, via spatula, bone and dumb-bell shapes towards almost straight-sided lobate strips. Whereas the corners of competent objects remain clear and are exaggerated during the heterogeneous deformation and 'horning' effect, the corners of incompetent objects become opened and smoothed, to virtually disappear.

Models with $m = 1$ and different n values (Fig. 9) provide the clue for the change in trend of competence noted in Fig. 7. Despite starting off with $m = 1$, and therefore by definition no viscosity or competence contrast, the $n = 3$ and 10 models appear to have become slightly incompetent objects as deformation proceeds (Fig. 9b and c). The reason for this is that all the FE models have a constant displacement rate (0.05 per time step for initial model dimension of 6), and this calibrates to an increase in strain-rate over progressive deformation. For example, when the model is 50% shortened ($R_B = 4$), its instantaneous strain rate is twice the strain rate of the first increment of deformation. This increase of strain rate does not, by definition, affect the viscosity of the linearly viscous matrix, or the object if linearly viscous (Fig. 9a), but it results in a lowering of the viscosity of the power-law objects (Fig. 9b and c) during progressive deformation. For example, we have an effective viscosity ratio (m'), of 0.63 for $n = 3$, and 0.53 for $n = 10$ at the instant of $R_B = 4$. These m' values decrease as deformation proceeds and the strain rates increase.

This property, i.e. a reduction in effective viscosity of the power-law objects as deformation proceeds, affects all our models to some extent, but only has a noticeable effect on the deformation in models with starting m values close to 1. This is the reason for the change in relative competence in the $m = 2$ model (Fig. 7) noted above. For a small deformation, the $n = 3$ and 10 objects behave more competently than $n = 1$, but at moderate to high deformation, they become less competent, because of the reduction in effective viscosity contrast (i.e. $m' < 2$). This is a property of FE modelling with non-linear rheology that would only be avoided by adopting a constant strain-rate, rather than constant displacement rate, in the models.

In Fig. 10, we compare object shapes for linear ($n = 1$) models over a wider range of m values (2–20), up to more extreme deformation than shown in Figs. 5–9. In addition to the four stages of deformation described for the preceding models, there are two additional increments with pure shear

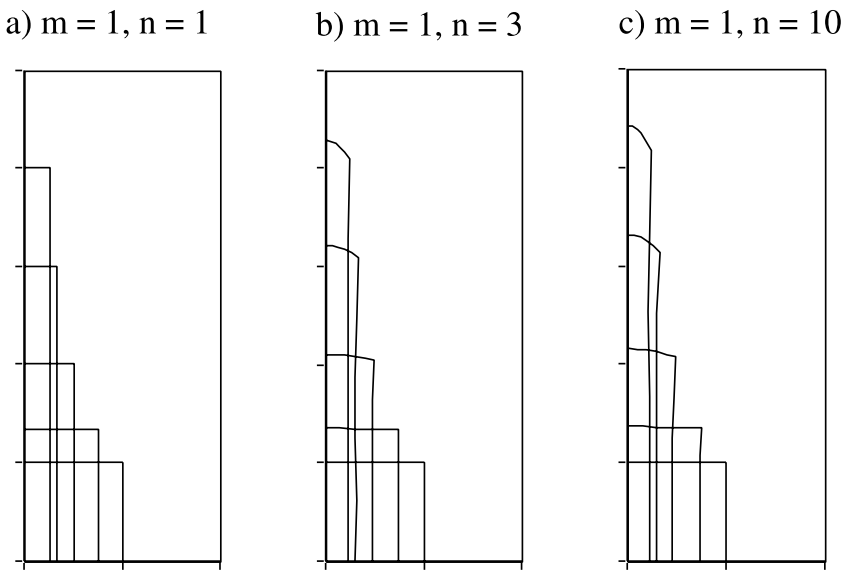

Fig. 9. Shape changes of square objects in a matrix in successive stages of pure shear with bulk pure shear strain ratios of $R_B = 1$ (initial square), 1.78 (25% shortening), 4 (50% shortening), 9 (67% shortening) and 16 (75% shortening), where there is no initial viscosity contrast ($m = 1$). (a) Object stress exponent (n) = 1, and the deformation is equivalent to that of a passive object, or the bulk deformation. (b) and (c) Progressive deformation of objects with initial $m = 1$ and $n = 3$ and 10, respectively. Note that these objects become progressively more incompetent, showing greater deformation than the bulk deformation and convex shortened edges. See text for discussion.

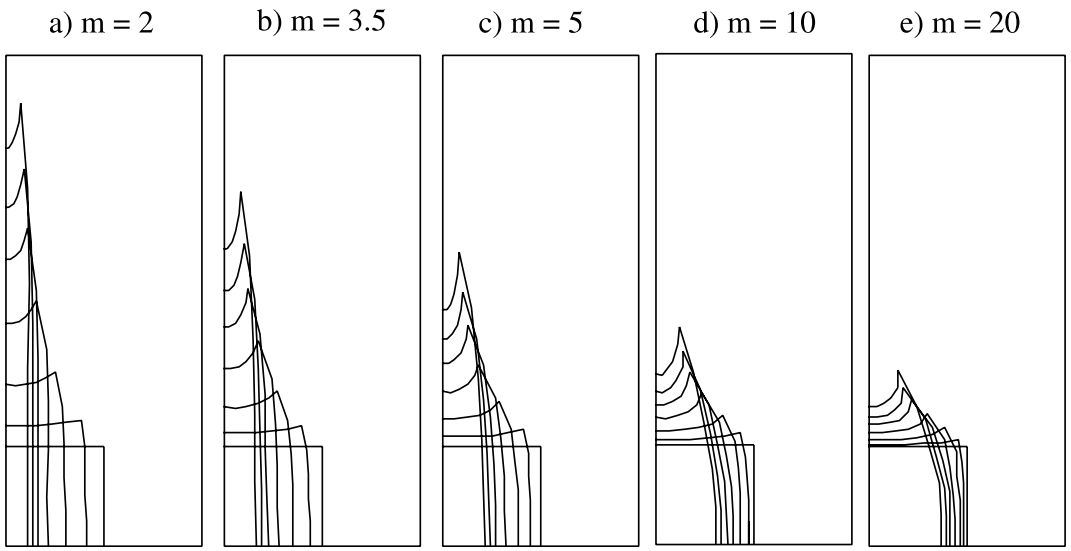

Fig. 10. Shape changes of Newtonian ($n = 1$) square objects in a matrix with viscosity ratios of $m = 2$–20, in successive stages of pure shear with bulk pure shear strain ratios of $R_B = 1$ (initial square), 1.78 (25% shortening), 4 (50% shortening), 9 (67% shortening), 16 (75% shortening), 23 (80% shortening) and $R_B = 32.7$ (82.5% shortening). All show variations of development of barrel shapes, 'fish mouths' and 'horns'.

strain ratio, $R_B = 23$ (80% shortening) and $R_B = 32.7$ (82.5% shortening). Such extreme deformation can only be achieved in this FE model when the object and matrix are both linear ($n = 1$). The purpose of this series (Fig. 10) is to examine the development of shape irregularity and end concavity in more detail, for analysis and in order to identify the m value that produced the greatest fish-mouth shape. When converted, by four-fold symmetry, into full barrel-shaped objects (e.g. Fig. 1a), these extreme stages of deformation have extremely concave shortened edges, and distinct horned and fish-mouth shapes, approaching some of the extreme shapes described for ductile geological boudins (e.g. Fig. 2). We will quantify the object concavity factors next, as these provide a possible method of estimating effective viscosity contrasts of geological objects with these shapes, such as fish-mouth boudins in a matrix.

4. Analyses: strain, shape irregularity and barrel or fish-mouth shapes

The strain and shape of the deformed objects in Figs 5–8 are analysed, following methods introduced by Treagus and Lan (2000). The object strain ratio, R_O, is defined as the axial ratio of the rectangle defined by the object corners (a/b, Fig. 11a). Although not a perfect measure of object strain, it is the best measure of gross object strain for competent barrel-shaped objects. However, it is not a very practical measure of the strain of the incompetent objects, because their corners are not clearly identifiable. Therefore, for $m = 0.1$, we define R'_O (a'/b', Fig. 11b), a measure of the maximum and minimum object dimensions. We defined an 'end shape factor', C, for objects (Treagus and Lan, 2000, fig. 16), where C is negative for concave-ended objects. It is

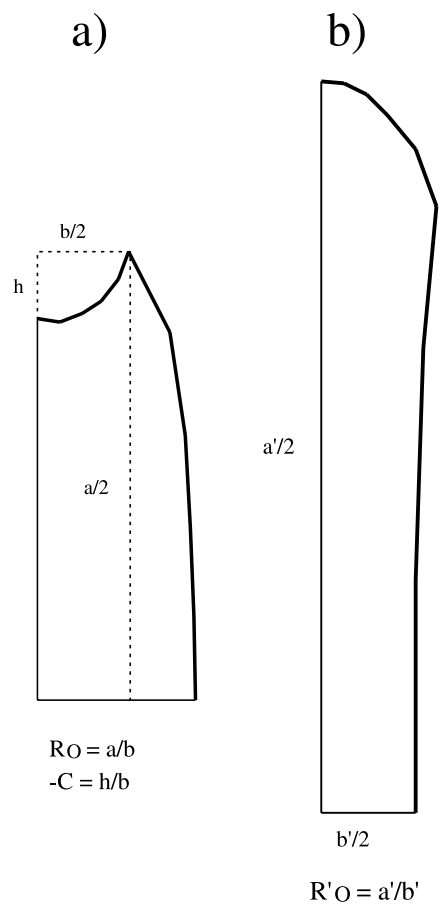

Fig. 11. Definitions for strain and shape analysis of deformed square objects, after Treagus and Lan (2000). (a) Object strain ratio for competent objects, $R_O = a/b$, the ratio of sides of the transcribing rectangle. Concavity factor, $-C = h/b$. (b) Object strain ratio for incompetent objects, $R'_O = a'/b'$ is a measure of the maximum and minimum object dimensions.

defined in Fig. 11c as h/b. These measurement parameters (R_O, R'_O, C) will be used for analysis and comparison of the models.

Fig. 12a shows R_O values vs. bulk strain (R_B) for the competent object models (Figs. 5–8), and R'_O for the incompetent models (Fig. 9). For all these models, R_O is only slightly decreased as n increases. The differences are most distinct for the $m = 5$ models. For the $m = 2$ models in Fig. 12, the slightly higher R_O values for $n = 1$ (than $n = 3$ or 10) appear to conflict with the appearance of greatest object strain for $n = 10$ for models in Fig. 7d, revealing that in this case, R_O (as defined in Fig. 11a) is not a perfect measure of the object strain. The R'_O values for the incompetent $m = 0.1$ models show the opposite: greatest strain for the highest n value modelled (i.e. $n = 10$). However, the differences between $n = 1$ and 3 are more significant than the differences between $n = 3$ and 10, which are very slight (~4% in R). In none of the models do the three n values result in R_O or R'_O values different enough to give overlapping curves in Fig. 12a, which would be indicative of marked changes in effective competence of objects with different n values but the same starting m values.

The results for $n = 1$ are compared with R_O and R'_O values for the earlier full square models of Treagus and Lan (2000, fig. 12a) in Fig. 12b. The full models have slightly larger R_O values of competent objects than the present quarter models, and moderately smaller R'_O values of incompetent objects. As shown in Fig. 3, the two sets of models have different object–whole model proportions (1/16 for the full model; 1/36 for this quarter model). The quarter models used here (also Treagus et al., 1996) provide a closer model to single objects in an 'infinite' matrix, or to very widely spaced objects, than do the full 'squares' models of Treagus and Lan (2000). (If modelling multiple objects, these would have diameter:centre spacing of 1/6, compared with the full models of 1/4.) It can be concluded from Fig. 12b that as the relative matrix area is decreased,

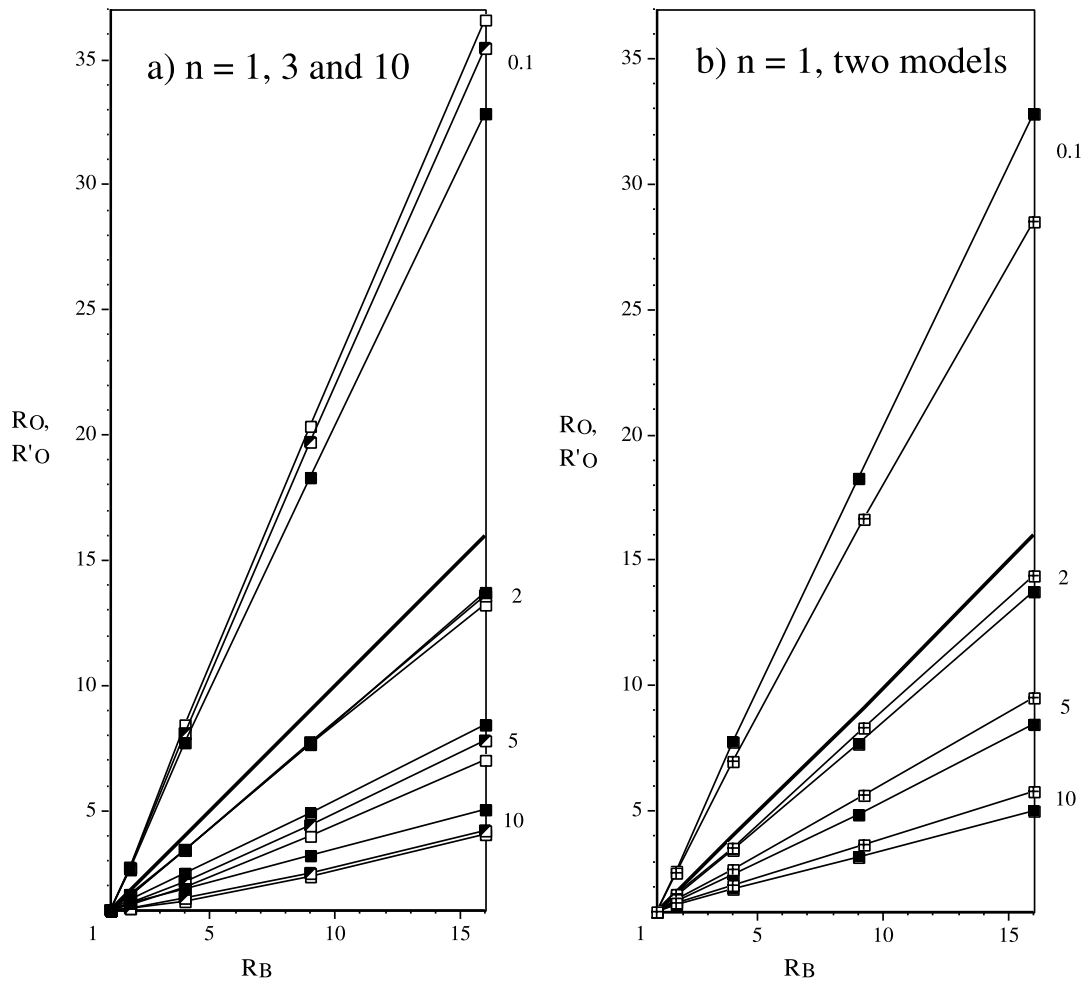

Fig. 12. Analyses of object strains. (a) R_O (competent objects) and R'_O (incompetent objects) vs. R_B in the models, with symbols indicating successive models shown in Figs. 5–8 with m values numbered 10, 5, 2 and 0.1. Objects with $n = 1$ are shown as solid squares, $n = 3$ as half-shaded squares, and $n = 10$ as open squares. (b) R_O (competent objects) and R'_O (incompetent objects) comparison of these quarter models with $n = 1$ with analyses of the full models of Treagus and Lan (2000) (cf. Fig. 2). Solid squares are the $n = 1$ models, as in (a); crossed squares are the earlier full models.

competent objects deform more tending towards the bulk deformation. Conversely, incompetent objects progressively deform less as they tend towards the bulk deformation. These model dimensions appear at least as important, or more, in determining object strain, as the variations in n values shown in Fig. 12a.

What is notable about all the strain measurements, whether R_O or R'_O, is that they are practically linear in Fig. 12. Similar linear curves were found by Treagus and Lan (2000), and were expressed as the approximate relationship: $(R_O - 1) = q(R_B - 1)$. The q factors are slightly different in the present models (slopes of lines in Fig. 12) from those in the earlier models, because of the differing object/matrix proportions in the full and quarter finite element models, discussed above. We have no simple explanation, mechanical or geometric, for this linear relationship.

Characteristic object shapes arise in competent and incompetent objects, as introduced in Fig. 1. The incompetent shapes are lobate and quasi-elliptical, and so are reasonably well described by the object strain measurement, R'_O, described above. However, the barrel and fish mouth shapes seen in the competent objects (Figs. 5–7) are a special feature of the shortened square edge of objects that are more viscous than their matrix, and these require a parameter in additional to R_O, to describe the shape irregularity. We use the concavity/convexity measure, C, defined in Fig. 11, where C is negative for concave-ended objects. A graph of concavity vs. bulk strain ($-C$ vs. R_B graph), as used by Treagus and Lan (2000, fig. 17), provides a measure of progressive object irregularity (Figs. 13 and 14). Fig. 13 compares $-C$ values for the $m = 10$, 5 and 2 models with $n = 1$, 3 and 10 (Figs. 5–7). The $m = 5$ models show the greatest $-C$-factor of the three sets, with the $n = 3$

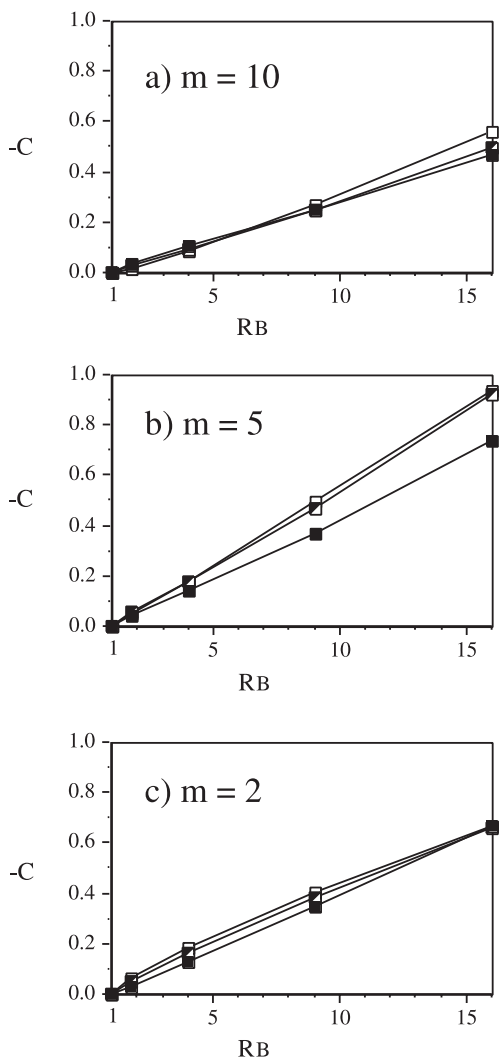

Fig. 13. Analyses of concavity ($-C$) of competent square objects versus bulk strain (R_B). Objects with $n = 1$ are shown as solid squares, $n = 3$ as half-shaded squares, and $n = 10$ as open squares. (a) $m = 10$; (b) $m = 5$; (c) $m = 2$.

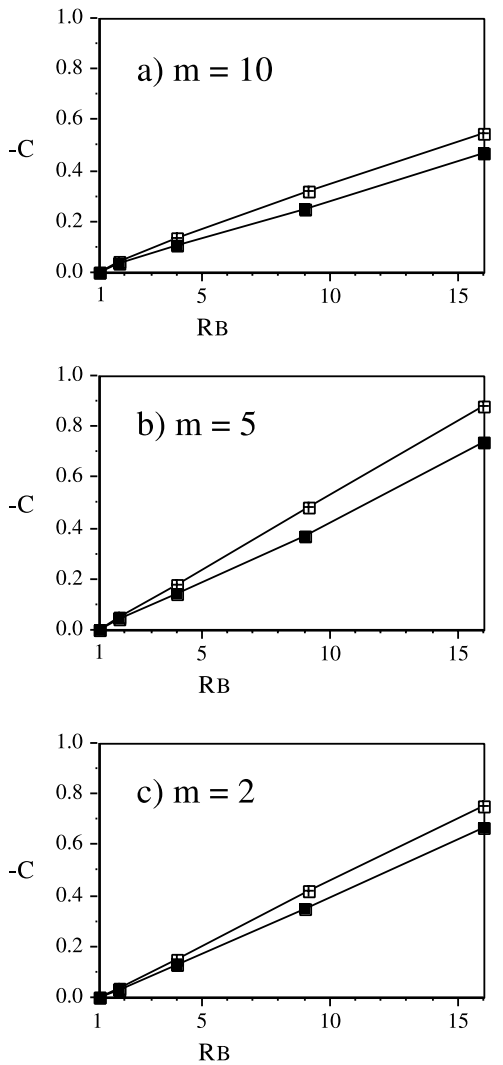

Fig. 14. Analyses of concavity ($-C$) of competent square objects vs. bulk strain (R_B): comparisons of quarter models with $n = 1$ (solid squares, as Fig. 13), with full models of Treagus and Lan (2000) (crossed squares). (a) $m = 10$; (b) $m = 5$; (c) $m = 2$.

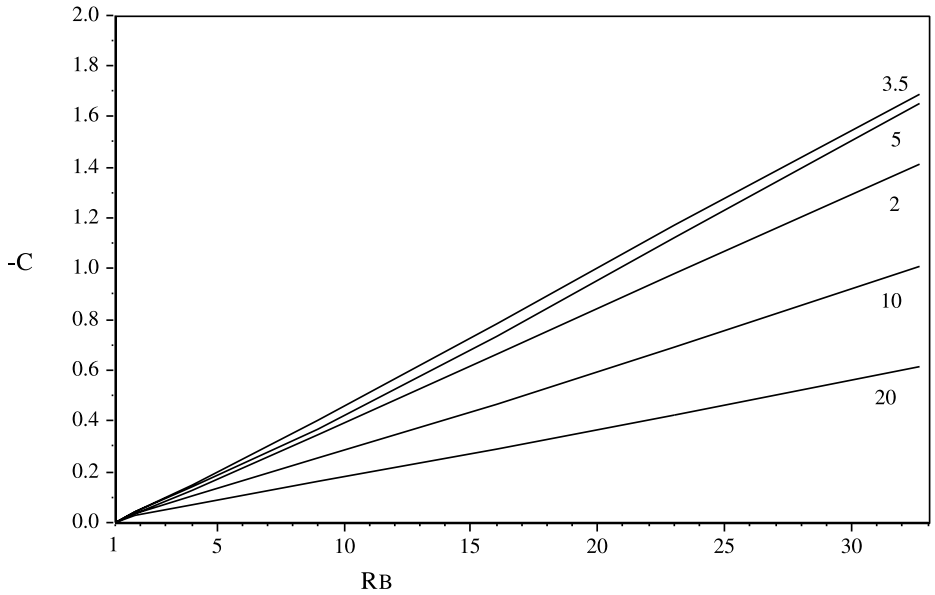

Fig. 15. Analyses of concavity ($-C$) of competent square objects vs. bulk strain (R_B) to higher strain, for the $n = 1$ models shown in Fig. 10. The maximum concavity is for $m = 3.5$.

and 10 models here giving measurably higher values than $n = 1$. There appears very little difference between $n = 3$ and 10, leading to a conclusion that the shape irregularity is not highly sensitive to the value of n. The curves in Fig. 13 are slightly non-linear for $n \neq 1$.

In Fig. 14, $-C$ versus R_B values are compared between the $n = 1$ quarter models of this paper, and the full square models of Treagus and Lan (2000). All the curves are very close to linear. For all three m values, the earlier models have a greater concavity factor, and the differences are as great, or more, than differences among different n values shown in Fig. 13. This is again confirmation that shape irregularity, as well as object strain discussed above, are related to the relative sizes of the objects and matrix. A smaller proportion of matrix means a greater concavity and shape irregularity.

Fig. 15 is an analysis of $-C$ versus R_B for the set of $n = 1$ models with object/matrix viscosity contrasts in the range of $2 \leq m \leq 20$, as shown in Fig. 10. Recall that these models included two further increments of deformation up to an extreme of $R_B = 32.7$ (82.5% shortening). We are interested in determining whether the greatest concavity factor is really found for $m = 5$, as deduced by Treagus and Lan (2000), or is some other m value between $m = 2$, 5 or 10. An investigation of numerous $n = 1$ models, with m varied by small amounts, reveals that $m = 3.5$ models (Fig. 10b) seem to show the maximum shape irregularity and $-C$-factor, and so this is taken for the limiting $-C$ values in Fig. 15. However, the C values are all very close for m values of 3–4, and the maximum may not be exactly $m = 3.5$ throughout progressive deformation. Fig. 16 shows the variation of $-C$ with $1 \leq m \leq 10$ for $n = 1$ models (e.g. Fig. 10) for bulk strain of $R_B = 9$ and 16. The maximum shape factor ($-C_{max}$) is close to $m = 3$ for $R_B = 9$, but at $m \approx 3.5$ for $R_B = 16$ and higher R_B values.

Note that all the curves in Fig. 15 are virtually linear, even at the highest deformation. As for the linear ($R_O - 1$) vs. ($R_B - 1$) graphs discussed above, there is no simple geometric or mechanical explanation for a linear relationship of C vs. ($R_B - 1$) for each m value, but it has some practical potential. For the linear models, the maximum shape irregularity (taken at $m = 3.5$) is given by $-C_{max} = (R_B - 1)/19$.

Comparison of Fig. 15 with Figs. 13 and 14, lead us to conclude that $-C_{max}$ values increase only slightly as object n values increase, and also increase (perhaps more

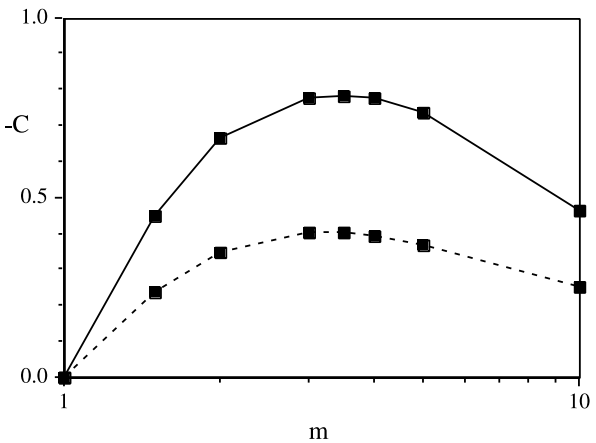

Fig. 16. $-C$ vs. m graph to determine the maximum concavity ($-C_{max}$) for models with bulk strain of $R_B = 9$ (lower broken curve) and $R_B = 16$ (upper solid curve): maxima are at $m \cong 3$ and 3.5, respectively. Symbols indicate models with $m = 1$, 1.5, 2, 3, 3.5, 4, 5 and 10 (all with $n = 1$), some of which are illustrated in Fig. 10.

significantly) as the relative object area increases. There is no reason to conclude that $-C_{max}$ would not remain close to $m = 3.5$ in these cases.

5. Geological discussion and conclusions

The finite element models of deformed square objects in a matrix reveal surprisingly small differences in object shape with object rheology. The non-linear power law competent objects with $n = 3$ and 10 deform as a whole slightly less (R_O values), and to slightly more irregular shapes (C values), than the linearly viscous ($n = 1$) object. However, the differences between $n = 3$ and 10 are so slight that they are insufficient to provide a practical criterion for characterising the rheology of natural square objects. The differences are even slighter for incompetent objects. It therefore seems unlikely that deformed square sectioned clasts or boudins will provide answers on whether the object deformed as a linearly viscous or power-law material. For the rest of the discussion, we will simply treat these objects as viscous and quasi-linear, and investigate their potential for measuring effective viscosity contrasts in rocks.

Our models and comparisons with earlier modelling (Treagus and Lan, 2000) reveal that the proportion of a square object to its matrix affects the degree and irregularity of object deformation. Competent objects in a smaller amount of matrix deform more (greater R_O), and more irregularly (greater $-C$), than quasi-isolated objects. In effect, spacing affects the competence of the objects. This property is not exclusive to square objects, but will be true for any shape, including elliptical objects (Mandal et al., 2003). It has obvious geological importance in rocks such as conglomerates, suggesting that if competent clasts are closer together they will deform more (less competently) than those in isolation. Object spacing therefore adds complexity to the use of geological square objects to determine viscosity contrasts of geological clasts or boudins.

Another question that concerns applications of these models to nature is whether it can be assumed that any geological clasts, or indeed boudins, were initially square. Different results are obtained if the initial shape is assumed to be rectangular with the long dimension parallel to the principal elongation. Although we have not undertaken comprehensive FEM of rectangular objects with a wide variation of aspect ratios, models with a 5:4 side ratio (elongate parallel to extension) reveal that these objects deform to shapes that have concavity factors ($-C$) about 10% greater than those for squares.

Lloyd and Ferguson (1981) used a rectangle with a 3:2 side ratio for FEM of elastic–plastic boudins. The ratio of 'boudin' to whole model is 1/6, considerably larger than our two sets of models (1/36 and 1/16), and the models are asymmetric, designed to simulate an inter-bodin gap between two rectangular boudins. Their model B2 (Lloyd and Ferguson, 1981, fig. 4), with a ratio of plastic yield strength (object–matrix) of 10, shows extreme horning and development of fish mouths with progressive deformation. This effect is asymmetric, being greater on the right edges of the 'boudin', which is close to the model edge, than on the left side which has double the matrix area.

Ramsay and Lisle (2000, fig. 39.19) also use a 3:2 rectangle with long axis parallel to extension, for FEM simulation of barrelling in boudins. The model has linearly viscous object and matrix (viscosity ratio, $m = 10$), but is only deformed to a bulk strain of $R_B = 2.56$ (compared with our models up to $R_B > 30$), so does not reveal extreme fish mouth shapes. Comparisons of the C values with our square models at the same bulk strain show that their rectangle short edge becomes significantly more concave than our square edge. However, these models also have a significantly larger object–whole model area ($\sim 1/3$), compared with our models (1/36), which will account for some of the difference, as well as the rectangular shape.

In the absence of any criterion to distinguish initially square from initially rectangular geological objects in nature, we will proceed with the assumption of equancy (squareness) for angular objects, by the same logic that round objects might be assumed to be originally circular. This assumption may not be correct for all boudins. Some might have initiated with rectangular form, but how rectangular is unknown, and if deformation is large enough the difference may not be too significant. We have not included any non-rectilinear geometry, such as might arise if boudins had formed by a process of 'necking'. Assuming initial squareness, as an approximation, allows us to estimate viscosity ratios and bulk strain for some examples of geological clasts and boudins with barrel to fish mouth shapes.

We return to the examples of boudinage shown in Fig. 2. The ductile deformation that gave rise to the barrelling (convexing of lengthening edges), and the concaved shortened edges with 'horning' and the 'fish mouth' or 'fish head' forms, is presumed to post-date the deformation that gave rise to the initial boudinage fracture, in all the examples. In the case of Fig. 2b and c, which are boudins in gneiss terrains, this ductile deformation is likely to have been large. Proceeding on the assumption that all the boudins were initially square in section, comparisons of their shapes can be made with the shapes for linear models in Fig. 10, and their concavity factors (C) as graphed in Fig. 15. This allows us to make estimates of the bulk ductile strain, and the effective viscosity ratios if both boudin and matrix are assumed linearly viscous, and have a coherent interface. These estimates also depend on the assumption that each boudin was 'isolated', rather than in close proximity with adjacent boudins, and neglecting any complex rheological variations in time or space that might be associated with localised deformation, metamorphism or recrystallisation. While all these assumptions may not be valid, if geologists are to make *any* attempt to quantify strain

in high-grade rocks with no convenient strain markers, or to quantify effective viscosity contrasts among different rock types, some unknowns must be simplified.

Fig. 2a shows a remarkably clear barrel-shaped boudin in calc–silicate rock in a marble matrix (Ramsay, 1967; Ramsay and Lisle, 2000). Its shape best matches the outline of the $m = 5$ example with $R_B = 4$ (Fig. 10c, step 2). The object has $-C$ value (Fig. 11a) of 0.15, which in Fig. 15 is the value for $m = 3.5$ or 5 for $R_B = 4$, but requires $R_B = 5.7$ for $m = 10$. There is no independent information in Fig. 2a to indicate the amount of ductile strain. We tentatively conclude that the barrelling of this boudin indicates a bulk ductile strain of $R_B \cong 4$ (50% shortening if plane strain), and that the calc–silicate boudin was about five times more viscous than the marble matrix.

The two boudins of amphibolite dykes in a quartzo-feldspathic gneiss matrix in Fig. 2b (Lloyd et al., 1982) are extremely 'horned' with fish mouth shapes, suggestive of a large ductile deformation. The $-C$ values of the four boudin ends range from 2 to 3. Given the extremity of this shape, we will assume that these represent $-C_{max}$ values, which will provide us with the lowest possible bulk strain estimate, assuming an 'isolated' square object and linear viscosity. This therefore assumes that the effective viscosity ratio of amphibolite to quartzo-feldspathic gneiss is $m \cong 3.5$. The relationship given earlier, $-C_{max} = (R_B - 1)/19$, leads to an estimate of $R_B = 39–58$. Although this appears a very large strain ratio, if converted to equivalent shear strains in a shear zone, it would be $\gamma = 6–7.5$. This amount of deformation may not be unreasonable for the complex deformational and metamorphic history of these Greenland gneisses (Wright et al., 1973).

Fig. 2c shows similarly extreme fish head boudins in amphibolite layers in quartzo-feldspathic gneiss matrix from an area of complex superposed deformation and migmatization in India (Ghosh and Sengupta, 1999). The two clearest fish mouths (Fig. 2c, left ends of right boudins) have $-C = 0.82$ and 0.85. If we again use the $-C_{max}$ relationship given above (assuming an effective viscosity ratio of amphibolite to quartzo-feldspathic gneiss of $m = 3.5$), we determine $R_B \cong 17$. This strain ratio may not be unreasonable in gneissic migmatised rocks, especially if accumulated from several phases of ductile deformation.

All these boudin examples suggest quite modest viscosity ratios of boudin to matrix, of 3.5–5. While these are based on a number of assumptions and approximations that may not all be valid, we can certainly conclude that these shapes would not arise if the viscosity ratios had been much higher. All the examples occur in metamorphic terrains where it might be assumed that ductility contrasts are different, perhaps smaller, than in equivalent sedimentary rocks (Ramsay, 1982). However, as noted in Section 1 (Introduction), similarly modest values (e.g. $m < 5$) for viscosity contrasts among a range of rock types have been deduced from studies of cleavage refraction (Treagus, 1999) and of conglomerates (Treagus and Treagus, 2002).

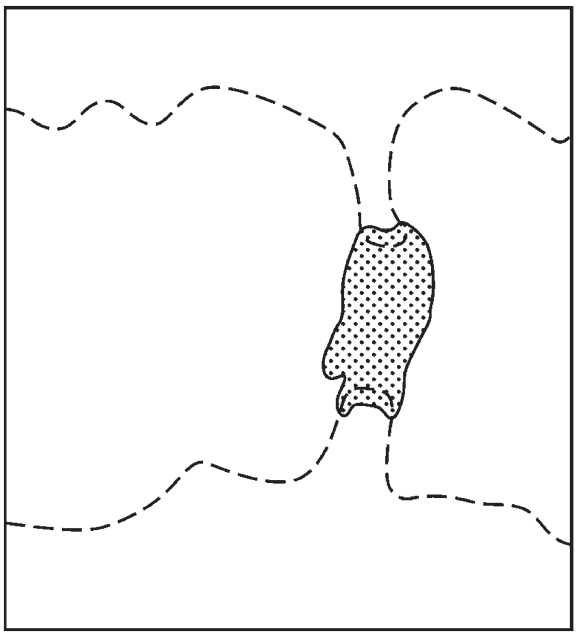

Fig. 17. Example of barrel-shaped plagioclase porphyroblast in quartz–muscovite matrix, from the Robertson River Metamorphics, Australia, after Johnson and Williams (1998, fig. 4a). The porphyroblast (length ~3.1 mm) is shaded, and the lower concave edge is used for analysis in the text. The traces of the schistosity surfaces showing the oppositely concave folds are shown by dashed curves.

We now consider whether these results are applicable to geological clasts of other kinds. Examples of barrel-shaped plagioclase porphyroblasts in a quartz–muscovite matrix are shown by Johnson and Williams (1998), although the emphasis in their paper is on 'oppositely concave folds'. Some of the porphyroblasts show distinctly concave shorted edges, and we will analyse one example (Johnson and Williams, 1998, figs. 3a and 4a) shown in Fig. 17. These authors deduced an elongation strain of $e = 1.76$ and a shortening of $e = -0.42$, which gives a strain ratio of $R_B = 4.7$. The concavity factor for the lower edge of the porphyroblast is $-C \cong 0.2$. These R_B vs. C values plot close to the $-C_{max}$ line, for $m = 3.5$, in Fig. 15, assuming a linearly viscous object. If we consider these values in comparison with our non-linearly viscous object (Fig. 13), an object with the range $m = 2$ or 5 and $n = 3–10$ is indicated. The strain ratio, R_O (Fig. 11a) for the porphyroblast (on the assumption that it was originally square) is $R_O = 3.6$. The R_O vs. R_B values compared with those in Fig. 12a indicate an m value a little more than 2. So for Fig. 17, on the basis of the strain calculations of Johnson and Williams (1998), the assumption of an initially square porphyroblast, and use of its aspect ratio and concavity, we estimate that the effective viscosity contrast of the plagioclase clast to quartz–muscovite matrix was $m = 2$ or 3. The plagioclase n value cannot be closely constrained, and could be in the range of 1–10.

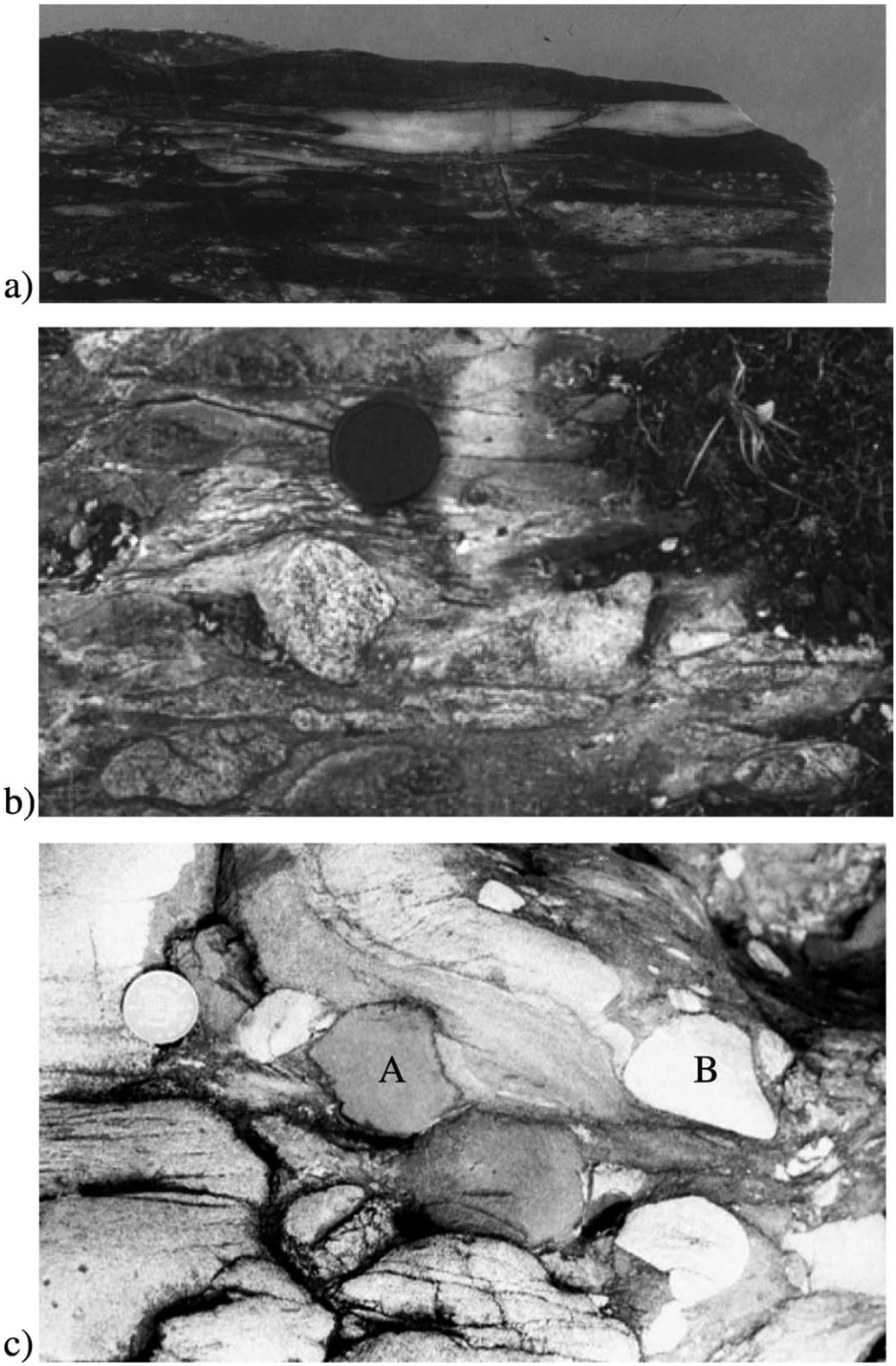

Fig. 18. Examples of clasts in conglomerates that have deformed to fish mouth, barrel or shield shapes, indicating a greater competence (viscosity) than the matrix or whole rock. All photographs taken with the trace of cleavage, and the stretching direction, horizontal on the page. (a) Fish mouth shape at the left end of pale clast (rhyolite) in polished specimen section of the Brioverian Cesson Conglomerate, Brittany, France (Treagus and Treagus, 2002). (Width of image 18 cm.) (b) Almost square barrel-shaped granite clast (below lens cap) in Ordovician Letterbrock Conglomerate, Co. Clare, Ireland. (Lens cap scale 5 cm diameter.) (c) Barrel and shield shaped psammite clasts (labelled A and B, respectively) in conglomerates of the Dalradian Easdale Slate, Benderloch, Argyll, Scotland. (Coin 2 cm diameter.)

Use of shape irregularity of angular clasts in breccia or conglomerate to determine rheology or viscosity contrast is more problematic. As noted in earlier discussion (Treagus and Lan, 2003), barrel or fish-mouth clasts appear to be rather rare in conglomerates, but isolated examples do occur (Fig. 18). When there is a single 'fish mouth' clast such as shown in Fig. 18a, it cannot necessarily be assumed that this was an original straight or square edge. Calculation of the C value (~ 0.8) for this clast, compared with the bulk strain value of $R_B = 7.3$ determined by strain analysis of this conglomerate (Treagus and Treagus, 2002), suggest that the shape is not consistent with a deformed square object. It is more likely that such extreme shape irregularity reflects an original concave face, or that this is a section of a clast with an irregular three-dimensional shape. Nevertheless, where concave faces are subparallel to the shortening direction in the rock, and convex faces parallel to extension, as shown for clasts in Fig. 18b and c, we can conclude that these might have been originally approximately square or rectangular, and are more competent than the matrix ($m > 1$). Shield-shaped clasts can also sometimes be observed, as illustrated in Fig. 18c, indicating deformation of a triangular object that is more viscous than the matrix. Even though these shapes may not be able to provide quantitative estimates of viscosity ratios among clasts and matrix, they might be able to provide qualitative information on viscosity contrasts.

Where the *competent* clasts in deformed conglomerates appear mainly to be quasi-elliptical, we conclude that the clasts must have been originally approximately circular or elliptical, since angular competent clasts will retain or exaggerate their angularity and irregularity during deformation. On the other hand, quasi-elliptical *incompetent* clasts in conglomerates could have originated with more angular shapes that have gradually disappeared during deformation and to become smoothed into quasi-elliptical shapes. Therefore, the combined analysis of deformed clast shapes and lithology in conglomerates may provide important clues to initial clast shapes and rheology.

Acknowledgements

This paper was begun while S.H.T. was in receipt of a NERC Senior Research Fellowship, which is gratefully acknowledged. As ever, Jack Treagus has provided constructive comments and advice, and he was instrumental in finding the examples of clasts shown in Fig. 18. John Dewey is thanked for information on the Letterbrock Conglomerate, and John Ramsay, Geoff Lloyd, Alan Wright, Sudipta Sengupta and Subir Ghosh are all thanked for providing information on boudins, and permission to use their photographs. We appreciate the review comments of Martin Casey and Nibir Mandal.

References

Carter, N.L., Tsenn, M.C., 1987. Flow properties of continental lithosphere. Tectonophysics 136, 27–63.

Cloos, E., 1947. Boudinage. Transactions, American Geophysical Union 28, 626–633.

Gay, N.C., 1968. Pure shear and simple shear deformation of inhomogeneous viscous fluids, 2. The determination of the total finite strain in a rock from objects such as deformed pebbles. Tectonophysics 5, 295–302.

Ghosh, S.K., 1993. Structural Geology. Fundamentals and Modern Developments. Pergamon Press, Oxford.

Ghosh, S.K., Sengupta, S., 1999. Boudinage and composite boudinage in superposed deformations and syntectonic migmatization. Journal of Structural Geology 21, 97–110.

Hanson, B.H., 1990. Thermal response of a small ice cap to climatic forcing. Journal of Glaciology 36, 49–56.

Hudleston, P.J., Lan, L., 1993. Information from fold shapes. Journal of Structural Geology 15, 253–264.

Hudleston, P.J., Lan, L., 1994. Rheological controls on the shapes of single-layer folds. Journal of Structural Geology 16, 1007–1021.

Johnson, S.E., Williams, M.L., 1998. Determining finite longitudinal strains from oppositely-concave microfolds in and around porphyroblasts: a new quantitative method. Journal of Structural Geology 20, 1521–1530.

Kirkby, S.H., Kronenberg, A.K., 1987. Rheology of the lithosphere: selected topics. Reviews of Geophysics 25, 1219–1244.

Lan, L., Hudleston, P.J., 1991. Numerical models of buckle folds in non-linear materials. Tectonophysics 199, 1–12.

Lan, L., Hudleston, P.J., 1996. Rock rheology and angular folds in single-layers. Journal of Structural Geology 18, 925–931.

Lan, L., Hudleston, P.J., 1997. Numerical simulation of fault-bend folds in fold-and-thrust belts. Proceedings of the 30th International Geological Congress V4, 106–118.

Lisle, R.J., Rondeel, H.E., Doorn, D., Brugge, J., van de Gaag, P., 1983. Estimation of viscosity contrast and finite strain from deformed elliptical inclusions. Journal of Structural Geology 5, 603–609.

Lloyd, G.E., Ferguson, C.C., 1981. Boudinage structure: some new interpretations based on elastic–plastic finite element simulations. Journal of Structural Geology 3, 117–128.

Lloyd, G.E., Ferguson, C.C., Reading, K., 1982. A stress transfer model for the development of extension fracture boudinage. Journal of Structural Geology 4, 355–372.

Mandal, N., Samanta, S.K., Bhattacharyya, G., Chakraborty, C., 2003. Deformation of ductile inclusions in a multiple inclusion system in pure shear. Journal of Structural Geology 25, 1359–1370.

Ramberg, H., 1955. Natural and experimental boudinage and pinch-and-swell structures. Journal of Geology 63, 512–526.

Ramsay, J.G., 1967. Folding and Fracturing of Rocks. McGraw Hill, New York.

Ramsay, J.G., 1982. Rock ductility and its influence on the development of tectonic structures in mountain belts. In: Hsü, K.J., (Ed.), Mountain Building Processes, Academic Press, London, pp. 111–127.

Ramsay, J.G., Lisle, R.J., 2000. The Techniques of Modern Structural Geology. Volume III. Applications of Continuum Mechanics in Structural Geology. Academic Press, London.

Rutter, E.H., 1993. The mechanics of natural rock deformation. In: Hudston, J.A., (Ed.), Comprehensive Rock Engineering, Pergamon Press, pp. 63–92.

Treagus, S.H., 1999. Are viscosity ratios measurable from cleavage refraction? Journal of Structural Geology 21, 895–901.

Treagus, S.H., Lan, L., 2000. Pure shear deformation of square objects, and applications to geological strain analysis. Journal of Structural Geology 22, 105–122.

Treagus, S.H., Lan, L., 2003. Simple shear of deformable square objects. Journal of Structural Geology 25, 1993–2003.

Treagus, S.H., Treagus, J.E., 2002. Studies of strain and rheology of conglomerates. Journal of Structural Geology 24, 1541–1567.

Treagus, S.H., Hudleston, P.J., Lan, L., 1996. Non ellipsoidal inclusions as geological strain markers and competence indicators. Journal of Structural Geology 18, 1167–1172.

Wegmann, C.E., 1932. Note sur le boudinage. Bull. Soc. Geol. France Ser 5 II, 477–491.

Wright, A.E., Tarney, J., Moorlock, B.S.P., Skinner, A.C., 1973. The geology of the Angmagssalik Area, East Greenland, and possible relationships with the Lewisian of Scotland. In: Park, R.G., Tarney, J. (Eds.), The Early Precambrian of Scotland and Related Rocks of Greenland, University of Keele, pp. 157–177.

Zienkiewicz, O.C., Taylor, R.L., 2000. The Finite Element Method: Volume 1. The Basis. Butterworth-Heinemann, Oxford.